

Markov chain Monte Carlo population synthesis of single radio pulsars in the Galaxy

Marek Cieślars,^{1*} Tomasz Bulik,² Stefan Osłowski^{3,4,5}

¹*Nicolaus Copernicus Astronomical Center, Polish Academy of Sciences, Bartycka 18, 00-716 Warsaw, Poland*

²*Astronomical Observatory, University of Warsaw, Al Ujazdowskie 4, 00-478 Warsaw, Poland*

³*Centre for Astrophysics and Supercomputing, Swinburne University of Technology, Hawthorn, Victoria 3122, Australia*

⁴*Fakultät für Physik, Universität Bielefeld, Postfach 100131, 33501 Bielefeld, Germany*

⁵*Max-Planck-Intitut für Radioastronomie, Auf dem Hügel 69, 53121 Bonn, Germany*

Accepted XXX. Received YYY; in original form ZZZ

ABSTRACT

We present a model of evolution of solitary neutron stars, including spin parameters, magnetic field decay, motion in the Galactic potential and birth inside spiral arms. We use two parametrizations of the radio-luminosity law and model the radio selection effects. Dispersion measure is estimated from the recent model of free electron distribution in the Galaxy (YMW16). Model parameters are optimized using the Markov Chain Monte Carlo technique. The preferred model has a short decay scale of the magnetic field of $4.27^{+0.4}_{-0.38}$ Myr. However, it has non-negligible correlation with parameters describing the pulsar radio luminosity. Based on the best-fit model, we predict that the Square Kilometre Array surveys will increase the population of known single radio pulsars by between 23 and 137 per cent. The *Indri* code used for simulations is publicly available to facilitate future population synthesis efforts.

Key words: stars: neutron – stars: statistics – pulsars: general – methods: numerical

1 INTRODUCTION

Evolution of neutron stars (NS) has been a subject of intense studies in the past. These objects are primarily observed as radio pulsars but can also be seen in other bands like the X-rays, gamma rays as well as in the optical range. There have been numerous efforts to model the radio population. Most notably the works of Narayan & Ostriker (1990), Faucher-Giguère & Kaspi (2006), Gonthier et al. (2007) then Kiel et al. (2008), Kiel & Hurley (2009), Osłowski et al. (2011) and in recent years Levin et al. (2013), Gullón et al. (2014), and Bates et al. (2014). For an in-depth review of population synthesis efforts see Popov & Prokhorov (2007) and Lorimer (2011).

We base our motivation to revisit the radio population of pulsars on the improved model of the electron density in the Galaxy Yao et al. (2017), and the availability of Markov Chain Monte Carlo (MCMC) to explore the multidimensional parameter space due to the extended computational power. We restrict our analysis to the evolution of the single pulsars from their birth in a supernova explosion to the moment they no longer can be detected in the radio waveband. We do not consider binary evolution and interactions there-

fore treatment of millisecond pulsars is beyond the scope of this paper. We do not simulate the full stellar and binary evolution that leads to formation of pulsars, such as was done by Kiel et al. (2008), Kiel & Hurley (2009) and Osłowski et al. (2011) and therefore we start with pulsars progenitor distribution as an input parameter to the simulation. We provide the *Indri* source code¹ with an intent that one can fully reproduce our results upon access to a small cluster², expand the scope of the simulation, use different data cuts or jump-start further development.

The paper is arranged as follows: in section 2 we explain the Galactic model, the kinematics of pulsar population, the evolution of the pulsars period and the magnetic field, luminosity models, the selection effects as well as the mathematical representation of the model, in section 3 we describe the construction of the likelihood of the model upon comparison with survey data and describe the implementation of the Metropolis-Hasting *MCMC* method, in section 4 we present the results obtained in the simulation, we discuss them in the section 5, and we summarize in section 6.

¹ The code can be obtained from the *GitHub* repository <http://github.com/cieslar/Indri>

² At the time of writing we define such machine as an approximately 200-cores cluster.

* E-mail: mcie@camk.edu.pl

2 THE MODEL

There are two broadly independent parts that are needed to describe the evolution of NSs. The first part is connected with the dynamical evolution of NSs in the gravitational potential of the Milky Way, and the second describes the intrinsic evolution in time of each neutron star as a radio pulsar. The model is roughly following the one presented by [Faucher-Giguère & Kaspi \(2006\)](#). In the following section we concentrate on the differences between our model and [Faucher-Giguère & Kaspi \(2006\)](#), while the identical components are presented in the Appendix A. We assume that the pulsars birth time has a uniform distribution. We model the evolution over a period of $t_{\max} = 50 \text{ Myr}$. It is important to note that the characteristic age $\tau = P/2\dot{P}$ can reach much higher values than t_{\max} because of the magnetic field decay (see discussion in [5.1.7](#)).

2.1 The Milky Way

2.1.1 The equation of motion - integration method

We use the *Verlet* method ([Verlet 1967](#)) to propagate pulsars through the Galactic potential. Following a Monte Carlo experiment (simulated motion of few millions of random pulsars), we found that the maximal time step can not exceed $dt_{\max} = 0.1 \text{ Myr}$ in order to limit the loss of the total energy to 1% due to the numerical errors. The actual time step dt_{act} is lower than dt_{\max} and it's equal to:

$$dt_{\text{act}} = \frac{t_{\text{age}}}{\frac{t_{\text{age}}}{dt_{\max}} + 1} \quad (1)$$

We discard pulsars which are more than 35 kpc away from the Galactic centre at the end of the simulation.

2.2 The neutron star physics

We assume constant values for the radius ($R_{\text{NS}} = 10 \text{ km}$), the mass ($M_{\text{NS}} = 1.4 M_{\odot}$) and the moment of inertia ($I_{\text{NS}} = 10^{45} \text{ g cm}^2$) of each neutron star.

2.2.1 The magnetic field decay

Following [Osłowski et al. \(2011\)](#) we assume that the magnetic field decays due to the Ohmic dissipation. For recent advanced we refer to the work of [Igoshev & Popov \(2015\)](#), though we simplify the time dependence of the decay to an exponential function. The decay model is parametrised by the time-scale Δ :

$$B(t) = (B_{\text{init}} - B_{\text{min}}) \exp\left(\frac{-t}{\Delta}\right) + B_{\text{min}} \quad (2)$$

To be consistent with our previous work [Osłowski et al. \(2011\)](#), and with [Kiel et al. \(2008\)](#), we use the minimum value of the magnetic field given by [Zhang & Kojima \(2006\)](#). We draw it from a log-uniform distribution:

$$10^7 \text{ G} < B_{\text{min}} < 10^8 \text{ G} \quad (3)$$

The results do not depend on the choice of B_{min} since the pulsars with such small magnetic field are not included in the comparison sample as they no longer emit in radio.

2.2.2 The evolution in time

The boundary conditions for the pulsars evolution are their initial and final magnetic field strength $B_{\text{init}}, B_{\text{min}}$ as well the spin period at birth P_{init} . To obtain a set of values P and B at the time t_{age} we integrate the radiating magnetic dipole (equation [A9](#)) by supplying it with the magnetic field decay (equation [2](#)):

$$P(t_{\text{age}}) = \frac{1}{\eta} \sqrt{2 \int_0^{t_{\text{age}}} (B^2(t) dt) + P_{\text{init}}^2} \quad (4)$$

where $\eta \simeq 3.2 \times 10^{19} \text{ G s}^{-1/2}$.

$$P(t_{\text{age}}) = \left(\frac{1}{\eta^2} \left((B_{\text{init}} - B_{\text{min}})^2 \left(1 - e^{-\frac{2t_{\text{age}}}{\Delta}} \right) \Delta + 4B_{\text{min}} (B_{\text{init}} - B_{\text{min}}) \left(1 - e^{-\frac{t_{\text{age}}}{\Delta}} \right) \Delta + 2B_{\text{min}}^2 t_{\text{age}} \right) + P_{\text{init}}^2 \right)^{\frac{1}{2}} \quad (5)$$

We obtain \dot{P} by inserting $P(t_{\text{age}})$ in equation [A9](#).

2.3 Radio Properties

2.3.1 The phenomenological radio luminosities

Since the first pulsar detection ([Hewish et al. 1969](#)), their radio emission process is still in debate ([Beskin et al. 2015](#)). In our work we assume a simple model of pair creation. Though, due to the phenomenological treatment of the luminosity it does not add any constraints, it is of significance only while considering the *death lines* (see section [2.3.2](#)). In this paper we use two different *a priori* assumptions about the radio luminosity.

The two-parameter power law. The general approach to describe the phenomenological relation between the P period, period derivative \dot{P} and the radio luminosity L_{ν} at frequency ν is a power law with two parameters α, β and a scaling factor γ see e.g. [Faucher-Giguère & Kaspi \(2006\)](#) and [Bates et al. \(2014\)](#):

$$L_{400, \text{p-1}} = \gamma P^{\alpha} \dot{P}^{\beta} \text{ mJy} \times \text{kpc}^2, \quad (6)$$

for the observational frequency $\nu = 400 \text{ MHz}$.

The rotational energy power law. A more restricted model is the one in which the luminosity is proportional to the rotational energy loss see e.g. [Narayan & Ostriker \(1990\)](#):

$$L_{\text{rot}} \equiv -\dot{E}_{\text{rot}} = \frac{4\pi^2 \dot{P}}{P^3}, \quad (7)$$

$$L_{400, \text{rot}} = \gamma \left(\dot{P}^{\frac{1}{3}} P^{-1} \right)^{\kappa} \text{ mJy} \times \text{kpc}^2. \quad (8)$$

We include the correction L_{corr} proposed by [Faucher-Giguère & Kaspi \(2006\)](#) and adopted by [Bates et al. \(2014\)](#) to both radio flux laws (eq. [6](#) and [7](#)):

$$\log L_{400} = \log \left(L_{400, \text{rot/p-1}} \right) + L_{\text{corr}} \quad (9)$$

The L_{corr} is randomly drawn from the normal distribution with $\sigma_{\text{corr}} = 0.8$ and accounts for spread of observed population around any parametric models of radio luminosity.

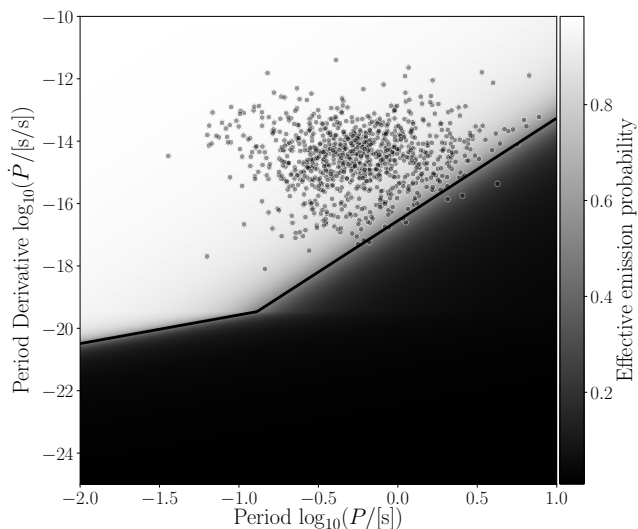


Figure 1. Death Area ($\mathfrak{D}_{\text{Area}}$) - the effective emission probability. Solid dark lines - canonical death lines ($\mathfrak{D}_{\text{Line}}$) by Rudak & Ritter (1994). Grey points - sub selection of ATNF catalogue used in the simulation.

We assume that the radio spectrum can be described by a power law:

$$L_\nu = L_{\nu_0} \left(\frac{\nu}{\nu_0} \right)^{\alpha_{\text{sp}}} \quad (10)$$

with the spectral index $\alpha_{\text{sp}} = -1.4$ (Maron et al. 2000). Pulsar emission is highly anisotropic. In order to model the geometry of the beam from a pulsar we incorporate the beaming factor following Tauris & Manchester (1998). For a pulsar with the period P we calculate the beaming fraction $f(P)$ in percent:

$$f(P) = 9 \times \left(\log \frac{P}{10\text{s}} \right)^2 + 3 \quad (11)$$

and determine the visibility of each pulsar assuming random orientation.

2.3.2 Death lines – death areas

In the canonical emission process (see Pacini 1967; Gold 1968) the radio waves are emitted due to the e^\pm pair creation and their acceleration and cascade creation in the presence of strong magnetic field. The pulsars radio emission process stops when the processes cannot be sustained (Rudak & Ritter 1994). These so-called *death-lines* are defined as:

$$\log \dot{P} = 3.29 \times \log P - 16.55, \quad (12)$$

$$\log \dot{P} = 0.92 \times \log P - 18.65. \quad (13)$$

Any pulsar crossing them during its evolution is considered radio inactive. However, such model contradicts the observations as a number of pulsars lie below these lines. This discrepancy can be attributed to the fact that death lines are devised for a specific structural model and parameters of the neutron star. Similarly to Arzoumanian et al. (2002), we

propose a phenomenological function to smooth the death lines into a continuous death area (see Figure 1). We propose a following formula:

$$\mathfrak{D}_{\text{Area}}(P, \dot{P}) = \frac{1}{\pi} \arctan \left(\frac{\log P - \mathfrak{D}_{\text{Line}}(\log \dot{P})}{\Psi} \right) + 0.5. \quad (14)$$

The value of Ψ parameter is set to 0.2 in order for the probability of radio activity to change in the range of $d \log P \sim 1$.

2.3.3 The dispersion measure

We compute the dispersion measure DM for each pulsar in the model population using the new and updated model of the electron density in the Milky Way (Yao et al. 2017, YMW16). The *Indri* code can also use the NE2001 model (see Cordes & Lazio 2002, 2003).

2.4 The computations

2.4.1 The mathematical representation

To mathematically represent the model we construct pulsar density in a three-dimensional space and smooth it with a Gaussian kernel. This *comparison space* is spanned by the period P , the period derivative \dot{P} and the flux at 1400 MHz, S_{1400} (shortened to S hereafter). The Gaussian averaged number of pulsars at a particular point (specified by indices k, l, m) of the *comparison space* $\log P_k - \log \dot{P}_l - \log S_m$ is expressed by:

$$\bar{\rho}_{klm} = \sum_b^{\text{PSR}} \frac{1}{(2\pi\sigma_{\text{cs}})^{\frac{3}{2}}} \exp \left(-\frac{(\log P_b - \log P_k)^2}{2\sigma_{\text{cs}}^2} \right) \exp \left(-\frac{(\log \dot{P}_b - \log \dot{P}_k)^2}{2\sigma_{\text{cs}}^2} \right) \exp \left(-\frac{(\log S_b - \log S_k)^2}{2\sigma_{\text{cs}}^2} \right), \quad (15)$$

where σ_{cs} is equal to 0.2. The particular value of the meta-parameter σ_{cs} has been heuristically chosen based on the behaviour of the model. Too low and the algorithm (described in section 3.2) would never converge. Too large and the model would reflect and find only the maximum of the three-dimensional distribution in the $\log P - \log \dot{P} - \log S$ space. To normalise the $\bar{\rho}_{klm}$ we use the sum R over all relevant points (located near observations):

$$R = \sum_{l,k,m} \bar{\rho}_{klm} \quad (16)$$

And then, construct the normalised, Gaussian averaged, pulsar density:

$$\rho_{klm} = \frac{1}{R} \bar{\rho}_{klm} \quad (17)$$

For the ease of notation we re-index the k, l, m indices with single i -index traversing all combinations of the k, l, m set. So that $\rho_i := \rho_{klm}$ represents a distinct point in the $\log P_k - \log \dot{P}_l - \log S_m$ space.

2.4.2 The performance of the evolutionary code

We have found that the main performance bottleneck in our computations is the evaluation of the dispersion measure in

the YMW16 model. The code provided by Yao et al. (2017)³ was not intended to be a part of a high performance computation and thus, we faced a choice. We could scale back the computation and abandon the *Monte Carlo* approach of the parameter search. Or we might make the galactic part of the model static losing the ability to test supernova kicks and initial position assumptions. We chose the latter option. The resulting algorithm is executed in two steps:

(i) We simulate the motion in the galactic potential (as described in the 2.1 section). The goal is to have one million neutron stars that are in the sky-window of the Parkes Survey. This number of pulsars is chosen for practical, computational reasons. We call this set of stars *the geometrical reference population*.

(ii) We take the *geometrical reference population* (the age, dispersion measure and distance) and use it as an input for physical computation (the 2.2 section). We use each NS from the *geometrical reference population* 5 times, i.e. we place five different model pulsars at each location, so that they have the same position in the sky and the same dispersion measure. The evolution computations finish with the radio-visibility test (the 2.3 section). We check whether the pulsar is beaming towards Earth and if it is emitting radio waves according to the death area criteria. If both conditions are satisfied we compute the luminosity L_{400} and the detected flux on Earth. To finish the test we check if the pulsars flux is higher than his minimal detectable flux. The population that satisfies the radio-visibility test is called *the model population*. This step ends with the computations of *the likelihood* statistic in the comparison space (see the 3.1.2 section).

The first step is done only once while the second step is used for the intensive *Monte Carlo* computations described in the following section. Such scheme allows us to investigate the model by using a population of five million pulsars. We note that should the YMW16 model be rewritten in computationally efficient way, it would be possible to carry out the simulation with the inclusion of a parametrisation of the initial positions, the SN kicks, and the Galactic potential.

3 COMPARISON WITH OBSERVATIONS

3.1 The observations

For the verification, we compare our model with a subset of the Australia Telescope National Facility Pulsar Catalogue⁴ (Manchester et al. 2005). We perform the following cuts to select an unbiased sample of pulsars:

- (i) we preselect single pulsars with measured necessary parameters (P , \dot{P} , S_{1400} , l , b , and DM),
- (ii) we choose only the pulsars that have been observed by the Parkes Multibeam Survey (Manchester et al. 2001),
- (iii) since we focus on the evolution of single pulsars we neglect the potentially recycled ones by requiring the inferred surface magnetic field to be greater than 10^{10} G.

³ We use the version 1.2.2 from www.xao.ac.cn/ymw16/

⁴ version 1.54, <http://www.atnf.csiro.au/research/pulsar/psrcat>

With these cuts we obtained a subset of 969 pulsars. In order to be consistent, we perform the second and third cuts as throughout *the model population* as well.

3.1.1 The comparison between model and observations

The pulsars density described in section 2.4.1 can be expressed for both the model ($\rho \rightarrow m$) or the observations ($\rho \rightarrow o$). For a given i -th point of the comparison space, we compare the model m_i pulsar density with the observed o_i pulsar density. Using the central limit theorem, we assume that the probability that the measured density o_i has its value given the model density m_i is described by a normal distribution:

$$\mathcal{P}_i(\bar{\theta}) = \mathcal{P}(m_i(\bar{\theta}), o_i) = \frac{1}{\sqrt{2\pi}} \exp\left(-\frac{(m_i(\bar{\theta}) - o_i)^2}{2}\right) \quad (18)$$

where we denoted the model parameters as $\bar{\theta}$. For numerical reasons, it more convenient to work with the logarithm of the probability \mathcal{P}_i :

$$\ln \mathcal{P}_i(\bar{\theta}) = -\ln(\sqrt{2\pi}) - \frac{(m_i(\bar{\theta}) - o_i)^2}{2} \quad (19)$$

3.1.2 Likelihood

In order to find optimal parameters for the model we use the likelihood statistic. In general, the likelihood \mathcal{L} of n independent variables x_1, \dots, x_n drawn from an unknown probability distribution parametrised by $\bar{\theta}$ is expressed by a joint probability function f :

$$\mathcal{L}(\bar{\theta}; x_1, \dots, x_n) = f(x_1, x_2, \dots, x_n | \bar{\theta}) \quad (20)$$

The joint probability function f is a product of probability functions g :

$$f(x_1, x_2, \dots, x_n | \bar{\theta}) = \prod_{i=1}^n g(x_i | \bar{\theta}). \quad (21)$$

In our case, due to the finite number of points in the comparison space, the independent variables x_1, \dots, x_n are represented by the points m_i (as defined in the section 2.4.1 and 3.1.1). The probability density function g is represented by \mathcal{P} (equation 18):

$$\mathcal{L}(\bar{\theta}) = \prod_{i \in \Omega} \mathcal{P}_i(\bar{\theta}) \quad (22)$$

where Ω denotes the set of points at which we calculate the pulsars density ρ_i . For our computation we use the logarithm of the likelihood:

$$\ln \mathcal{L}(\bar{\theta}) = \sum_{i \in \Omega} \ln \mathcal{P}_i(\bar{\theta}) \quad (23)$$

3.2 Markov chain Monte Carlo

To find the most probable parameters of the model we use the *Markov chain Monte Carlo* technique (MCMC). For the discussion of this widely used and established concept we refer to the works of Tarantola (2005), MacKay (2003) or Sharma (2017). In our case, we use the *Metropolis-Hastings* random walk (Hastings 1970) approach to construct chains of likelihood values. At the start of each chain, the parameter vector $\bar{\theta}$ is randomly drawn from the whole available

parameters subspace (see Table 1 and section 4 for parameters definitions) using a flat distribution in each dimension. During the random walk phase, the new set of parameters is drawn according to the normal probability distribution centered at the old set of parameters. The drawing is done independently for each i -th parameter:

$$P(\theta_n^i, \theta_p^i) = \frac{1}{\sqrt{2\pi\sigma_{\theta^i}^2}} \exp\left(-\frac{(\theta_n^i - \theta_p^i)^2}{2\sigma_{\theta^i}^2}\right) \quad (24)$$

where the σ_{θ^i} is set to a $\frac{1}{3}$ -th of the parameter interval (for the interval description see Table 1). To draw parameters whose initial distribution is log-normal, we replace the value of the parameter with its logarithm in equation 24. If the newly drawn parameter is outside of bounds the procedure is repeated. Following the methodology presented by Mosegaard & Tarantola (1995) we use the likelihood-modified step function to decide if the chain will move to the next location in the *Metropolis-Hastings* algorithm:

$$\mathcal{R}_{pn} = \frac{\mathcal{L}(\bar{\theta}_n)}{\mathcal{L}(\bar{\theta}_p)} \quad (25)$$

where p and n denote the *previous* and *next* set of parameters $\bar{\theta}$ of a given step. If $\mathcal{R}_{pn} \geq 1$, the jump is certain. If it is $\mathcal{R}_{pn} < 1$ then a jump to *next* set of parameters is done with the probability equal to \mathcal{R}_{pn} . The calculations are repeated until the distribution of chain end-points becomes subjectively stable.

3.2.1 Optimization and verification of the MCMC

We have learnt that some of the Markov chains converge on the maximum too slowly or not at all (should they be initially located too far from the extrema in the parameter space). This is well known, general problem of MCMC methods. It differs between algorithms and techniques and can be, depending on the technique, minimized to some extent. Instead of implementing more sophisticated method (see Gilks et al. 1995; Foreman-Mackey et al. 2013), we did two kinds of simulations. A general one, with a broad step-size to pinpoint the general area of the maximum of the likelihood (as described in previous subsection). And a second one, starting from a single point in the vicinity of the maximum of likelihood with four times smaller step-size (a $\frac{1}{12}$ -th of the parameter interval described in Table 1). We have run 1000 chains, each 5000-links long. We confirmed that the chains reach stability by computing the integrated autocorrelation time IAT⁵ (see Goodman & Weare 2010). The maximum IAT values, among all marginal parameters distributions, were 279 and 176 links for the *power-law* and *rotational* model, respectively.

4 RESULTS

We limited our studies to two models – the *power-law* and the *rotational* model. They differ in the phenomenological description of the radio luminosity (see section 2.3.1). To

⁵ We used the procedure *acor* from the <https://github.com/dfm/acor> repository.

| Parameter | Min value | Max value | Space |
|-------------------------------|-------------|------------|-------|
| α | -2. | 2. | 1 |
| β | -0.5 | 1. | 1 |
| κ | 0.2 | 1.4 | 1 |
| γ mJy | 10^{-4} | 10^4 | log |
| Δ Myr | 10^0 | 10^2 | log |
| $\widehat{B}_{\text{init}}$ G | 10^{12} | 10^{13} | log |
| $\sigma_{B_{\text{init}}}$ G | $10^{0.25}$ | $10^{0.7}$ | log |
| $\widehat{P}_{\text{init}}$ s | 0.01 | 0.6 | 1 |
| $\sigma_{P_{\text{init}}}$ s | 0.01 | 0.6 | 1 |

Table 1. The constraints of the parameters. The *Space* column indicates whether the parameters axis is linear or logarithmic. It also correspond to the parameters jump probability distribution – normal or log-normal, respectively. The α , β , and κ parameters are dimensionless.

describe them, we use a 8 (for the power-law model) or 7 (for the rotational model) parameters listed in Table 1. Four of the parameters are used to describe the initial conditions: distributions of magnetic fields ($\widehat{B}_{\text{init}}$, $\sigma_{B_{\text{init}}}$) and periods ($\widehat{P}_{\text{init}}$, $\sigma_{P_{\text{init}}}$). One parameter (Δ) is associated with the decay scale of the magnetic field. And the remaining three (γ , α , β) in case of the *power-law* or two (γ , κ) in the *rotational* model describe the radio luminosities.

4.1 The parameters marginal space

To visualize the multidimensional parameter space, we present one and two dimensional marginalised posterior distributions. The two dimensional results for *power-law* and *rotational* models are presented in Figures 2 and 3, respectively. The one-dimensional marginalised posterior distributions are shown in Figure 4.

4.1.1 The marginal distribution

The *two-dimensional* marginal probability distribution of the i -th and j -th parameters (denoted as $\mathcal{D}_{\theta_{ij}}$) is expressed by marginalizing the full-dimensional probability distribution $\mathcal{D}_{\bar{\theta}}$ upon all other parameters (Ω' represents the parameter space excluding i -th and j -th dimensions):

$$\mathcal{D}_{\theta_{ij}} = \int_{\Omega'} \mathcal{D}_{\bar{\theta}} d\Omega' \quad (26)$$

Similarly, the *one-dimensional* marginal distribution of the i -th parameter \mathcal{D}_{θ_i} is expressed by:

$$\mathcal{D}_{\theta_i} = \int_{\Omega''} \mathcal{D}_{\bar{\theta}} d\Omega'' \quad (27)$$

where Ω'' represents the parameter space excluding all but the i -th dimension. To obtain the continuous probability density function ($\mathcal{C}_{\theta_{ij}}$ and \mathcal{C}_{θ_i}) of the marginal distribution ($\mathcal{D}_{\theta_{ij}}$ and \mathcal{D}_{θ_i}) we use the Gaussian kernel density estimation method (Scott 2015) with a bandwidth h (a function of number of points n and dimensions d):

$$h(n, d) = n^{\frac{-1}{d+4}}, \quad (28)$$

4.1.2 The most probable value and significance levels

We denote the *most probable value* (MPV) – the maximum of the marginal, continuous probability density function for

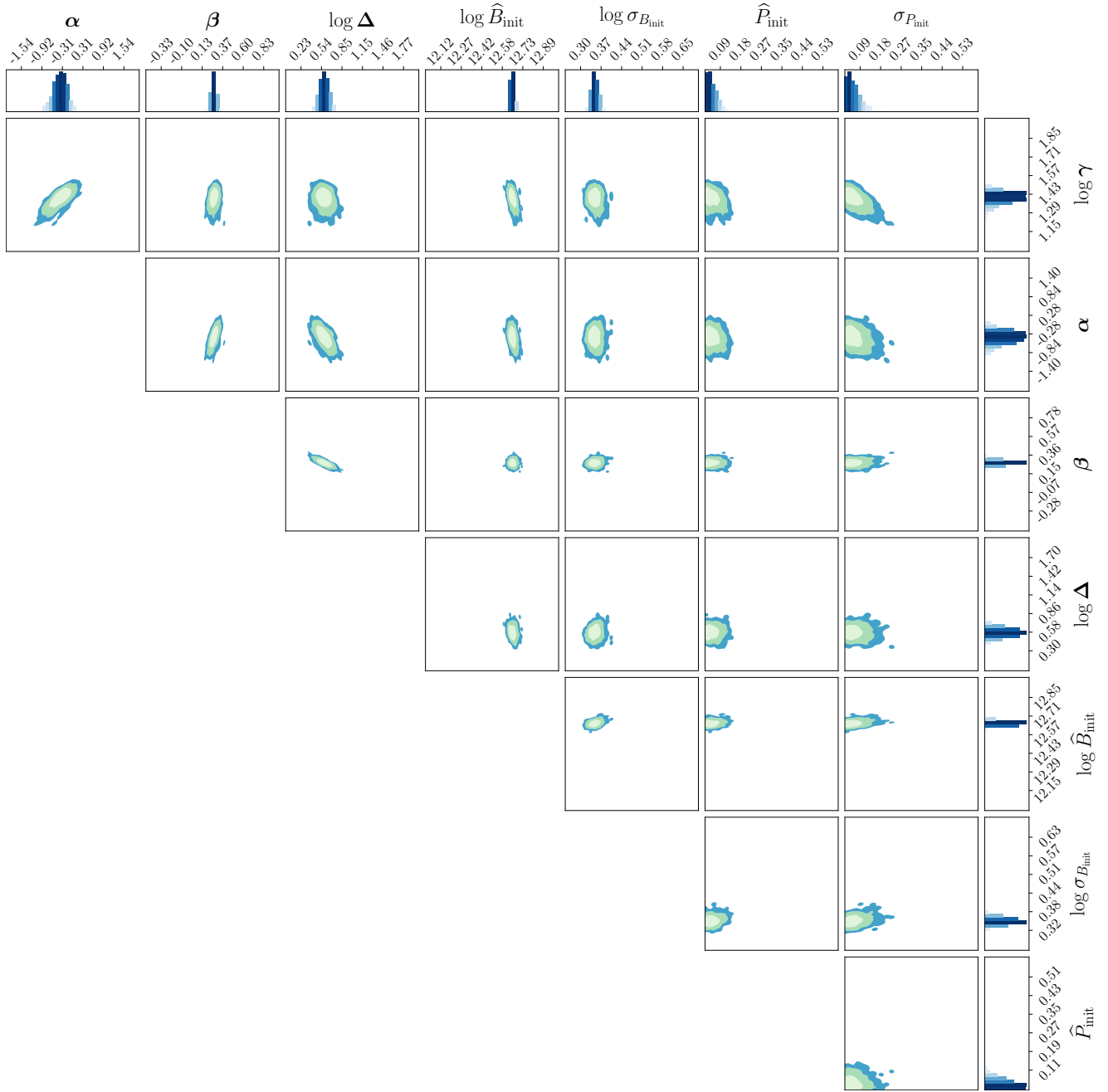


Figure 2. The *power-law* model – MCMC marginal parameter space. The 1D marginal distribution express the auto-scaled, normalised probability density $dN/(Ndi)$ where i is appropriate parameter according to the plot. On the 2D contour plot the colours represent the 1, 2, 3 – σ levels. We constrained the range of the γ posterior to zoom in on the populated part of the phase space.

each parameter (see Table 2). For confidence levels we use the 1, 2, 3 – σ ranges corresponding to the 68.27, 95.45, and 99.73 per cent of the distribution. The σ ranges are computed by integrating the probability around the MPV.

4.1.3 Correlation coefficients

In the Table 3 we present the linear correlation coefficient r :

$$r = \frac{\sum_{i=1}^n (x_i - \bar{x})(y_i - \bar{y})}{\sqrt{\sum_{i=1}^n (x_i - \bar{x})^2} \sqrt{\sum_{i=1}^n (y_i - \bar{y})^2}} \quad (29)$$

for both models for each pair of the parameters, where n is the number of chains in the final analysis.

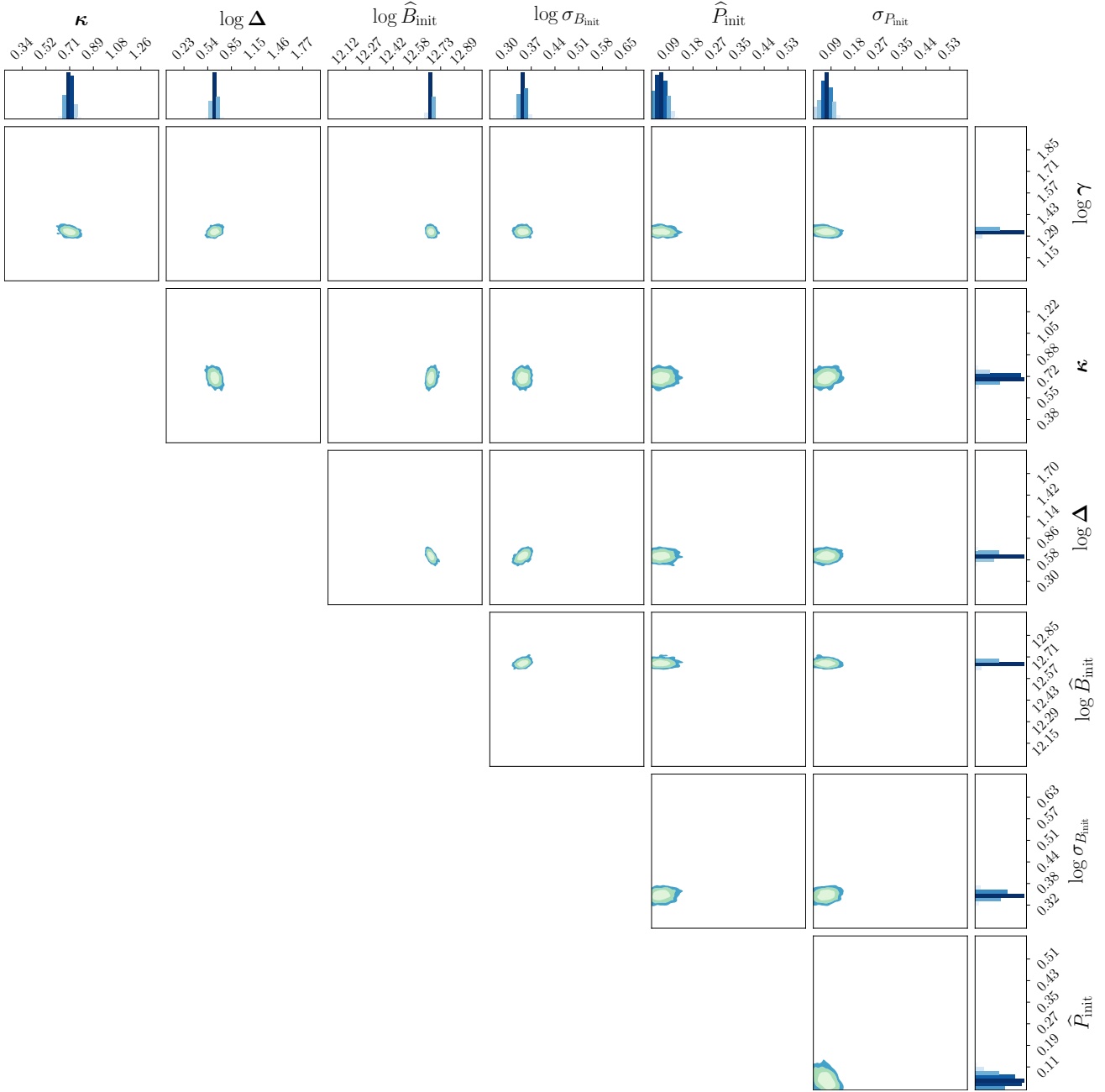


Figure 3. The *rotational* model – MCMC marginal parameter space. The 1D marginal distribution express the auto-scaled, normalised probability density $dN/(Ndi)$ where i is appropriate parameter according to the plot. On the 2D contour plot the colours represent the 1, 2, 3 – σ levels. We constrained the range of the γ posterior to zoom in on the populated part of the phase space.

4.2 The resulting population

For both sets of the MPVs (for the *power-law* and *rotational* models) we computed a population of pulsars. We show the visible in the Parkes Multibeam Survey part of the population of the Figure 5. The method of presenting the pulsar density in two dimensional marginalisations of the comparison space (P - \hat{P} - S) is the final verification of the obtained results. As can be seen in the second row for the *power-law* model and in the third row of the Figure 5 for the *rotational*

model, the fit of the modelled data to the observations can not be considered incorrect. We note that our simulation scheme always under estimates the data density – this behaviour can be seen as the pulsars density does not encompass the corresponding contour lines of the observations.

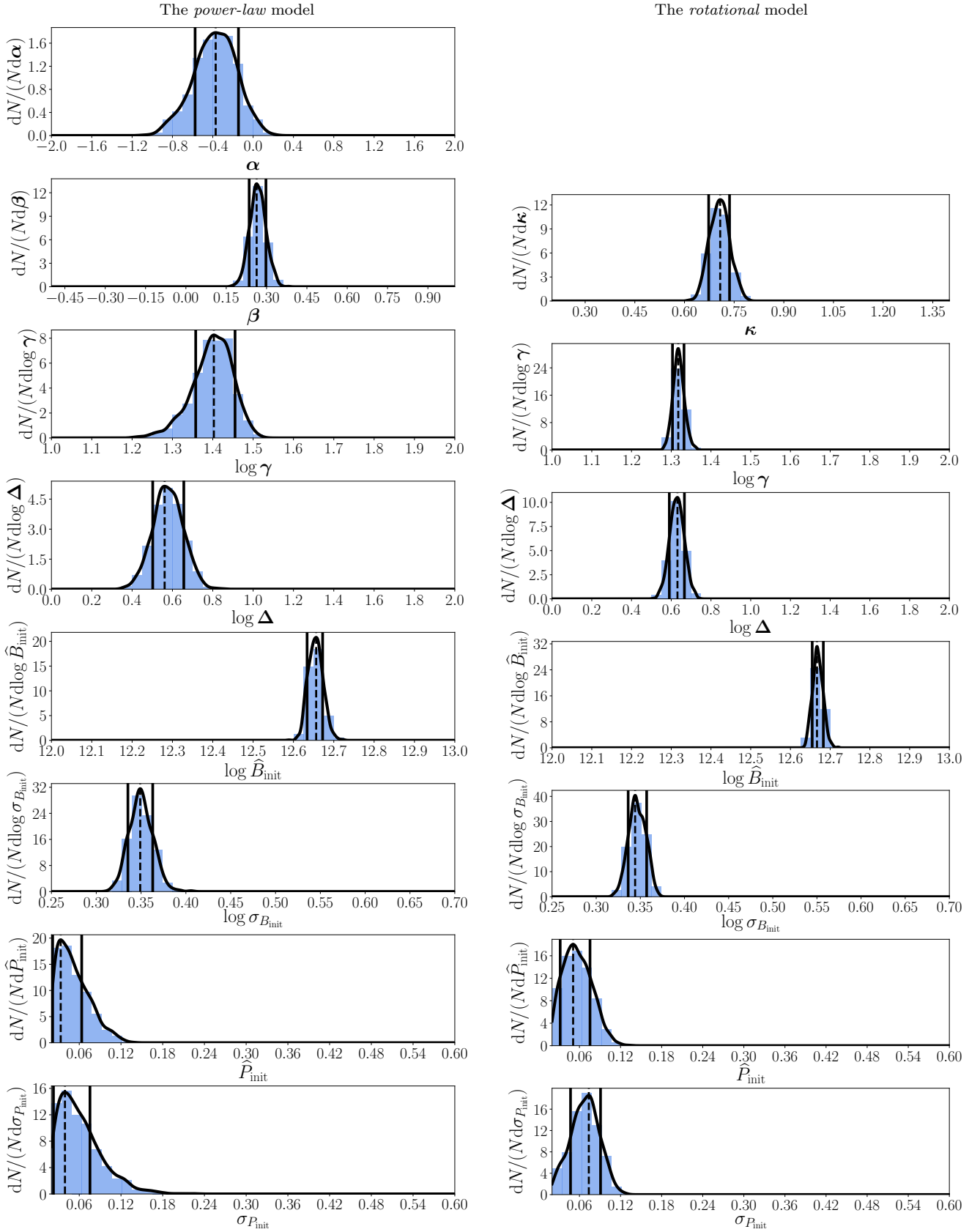


Figure 4. The comparison of the marginal distributions for both models. The 1-sigma level is derived by using Gaussian Kernel Density Estimation (black line) by integrating the probability from the Most Probable Value (dotted line). We constrained the range of the γ posterior to zoom in on the populated part of the phase space.

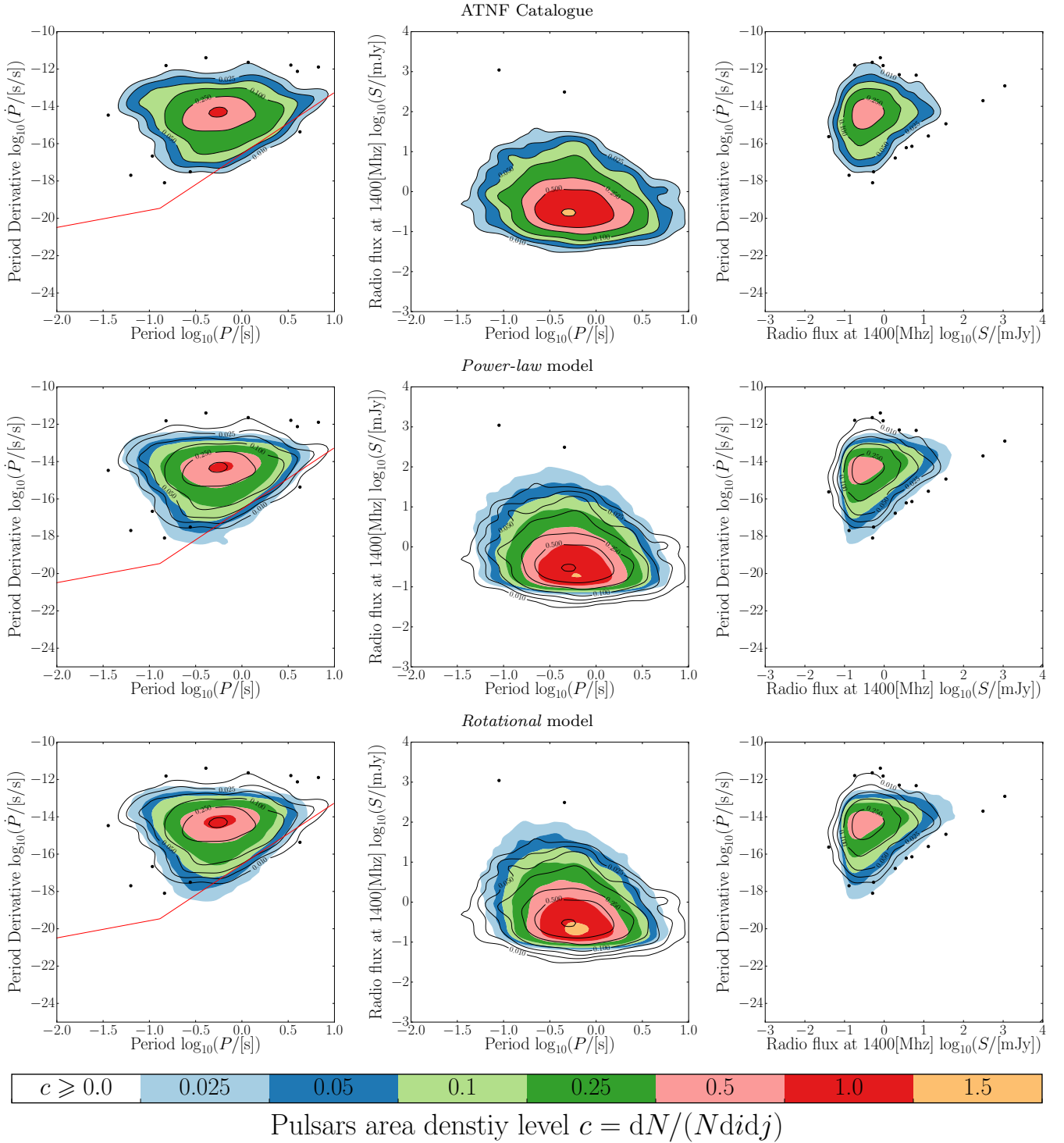


Figure 5. Observations – the subset of the ATNF catalogue (first row), *power-law* model (second row), and *rotational* model in the two-dimensional marginalisations of the comparison space P - \dot{P} - S . The colours indicate density levels for a given pair of dimensions i, j (for e.g. $i = P$ and $j = \dot{P}$ for the first column). The contour lines relate to the observations in each plot. The dots represent observations that lay in the region with extremely low density.

5 DISCUSSION

5.1 The model

5.1.1 Initial period distribution

We reached quite narrow initial period parameter distributions with most probable values equal to: $\hat{P}_{\text{init}} \approx 0.03$ s and

| Parameter | Most Probable Value |
|--|-------------------------|
| <i>power-law model</i> | |
| α | $-0.37^{+0.22}_{-0.21}$ |
| β | $0.26^{+0.04}_{-0.02}$ |
| $\log(\gamma/\text{mJy})$ | $1.40^{+0.06}_{-0.04}$ |
| $\log(\Delta/\text{Myr})$ | $0.56^{+0.10}_{-0.06}$ |
| $\log(\widehat{B}_{\text{init}}/\text{G})$ | $12.66^{+0.01}_{-0.03}$ |
| $\log(\sigma_{B_{\text{init}}}/\text{G})$ | $0.35^{+0.01}_{-0.01}$ |
| $\widehat{P}_{\text{init}}$ s | $0.03^{+0.03}_{-0.01}$ |
| $\sigma_{P_{\text{init}}}$ s | $0.04^{+0.04}_{-0.02}$ |
| <i>rotational model</i> | |
| κ | $0.71^{+0.03}_{-0.04}$ |
| $\log(\gamma/\text{mJy})$ | $1.32^{+0.01}_{-0.02}$ |
| $\log(\Delta/\text{Myr})$ | $0.63^{+0.04}_{-0.04}$ |
| $\log(\widehat{B}_{\text{init}}/\text{G})$ | $12.67^{+0.01}_{-0.02}$ |
| $\log(\sigma_{B_{\text{init}}}/\text{G})$ | $0.34^{+0.02}_{-0.01}$ |
| $\widehat{P}_{\text{init}}$ s | $0.05^{+0.03}_{-0.02}$ |
| $\sigma_{P_{\text{init}}}$ s | $0.07^{+0.02}_{-0.02}$ |

Table 2. The most probable values (MPV) with one- σ confidence level (the upper and lower limit). The α , β , and κ parameters are dimensionless.

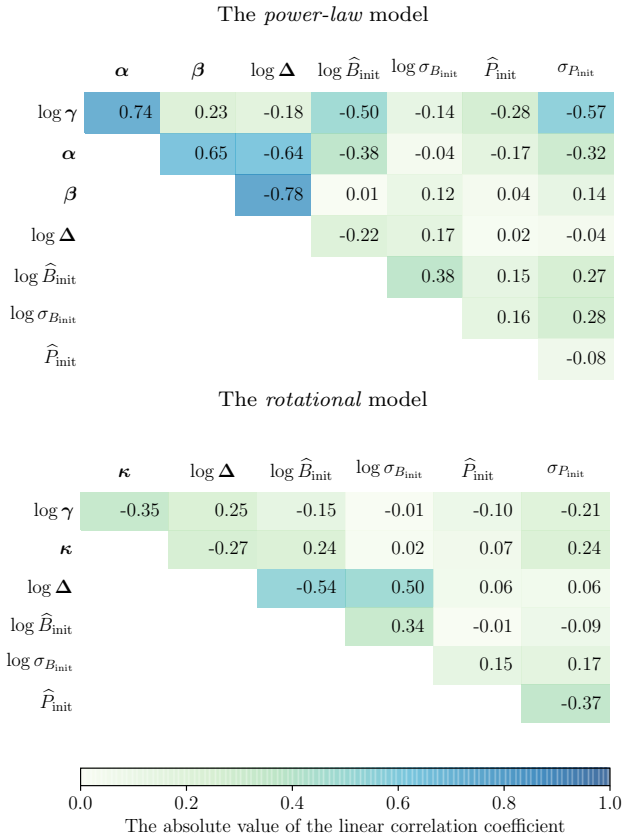


Table 3. The linear correlation coefficient matrices. The colour represent the absolute value of correlation coefficients.

0.05 s for the *power-law* and *rotational* model, respectively. They both cover similar range of values but the preferred mean value for the *power-law* model is significantly lower. In case of the standard deviation parameter of the initial period distribution we found out to be the most likely: $\sigma_{P_{\text{init}}} \approx 0.03$ s and 0.07 s for the *power-law* and *rotational* model, respectively.

The resulting distributions of initial periods in both cases are in agreement with the predictions made by [Blondin & Mezzacappa \(2007\)](#). However the hydrodynamic simulations lead to contradictory results ([Rantsiou et al. 2011](#)). In comparison to other population synthesis, in the works of [Popov et al. \(2010\)](#) they concluded that $\widehat{P}_{\text{init}} \approx 0.25$ s with $\sigma_{P_{\text{init}}} \approx 0.0001$ s, while [Faucher-Giguère & Kaspi \(2006\)](#) obtained the values $P_{\text{init}} = 0.3$ s and $\sigma_{P_{\text{init}}} = 0.15$ s. The main difference between our results and [Faucher-Giguère & Kaspi \(2006\)](#) is the inclusion of magnetic field decay which can be interpreted as an accelerator for the pulsar movement on the $P-\dot{P}$ plane. Thus, the population can have faster initial periods as it evolves to the same final population. Moreover, [Popov et al. \(2010\)](#) included the magnetic field decay and reached similar values as [Faucher-Giguère & Kaspi \(2006\)](#). Therefore, we are convinced the discrepancy with previous results is due to better sampling of the parameter space. In particular, we evaluated a larger number of models and didn't manually constrain the prior ranges.

5.1.2 Initial magnetic field distribution

The distribution of initial magnetic fields is almost identical in both models with the mean $\log B_{\text{init}} \approx 12.66$ and $\log \sigma_{B_{\text{init}}} \approx 0.34$). Those results are consistent with findings of [Faucher-Giguère & Kaspi \(2006\)](#) where they obtained $\log B_{\text{init}} = 12.65$ and $\sigma_{B_{\text{init}}} = 0.55$. In the work of [Popov et al. \(2010\)](#), authors reached larger value of the mean $\log B_{\text{init}} = 13.25$ with $\sigma_{B_{\text{init}}} = 0.6$. Such initial distribution of values means that no pulsar has initial field less than $\log B_{\text{init}} \approx 11$. Such conclusion is consistent with the fact that if such pulsars with low magnetic field strength existed they would be clearly observable in the radio band. Furthermore, their evolution would be very slow which would increase their detection probability. The lack of observed pulsars in the region of $P \approx 0.1$ s and $\dot{P} \approx 10^{-17} - 10^{-18}$ ss^{-1} implies that no quick spinning pulsars with magnetic field below $\log B_{\text{init}} \approx 11$ are formed.

5.1.3 The rotational radio-emission model

In the *rotational* model we obtained the value of the exponent κ in range between 0.67 and 0.74. Upon translating to L_{rot} (see eq. 7), we see that its exponent $\frac{1}{3}\kappa$ ranges from 0.22 to 0.24. This result disagrees with values obtained by [Gullón et al. \(2014\)](#) in the range from 0.45 to 0.5. We suspect that not including any radio switch-off mechanism (e.g. death lines) and limiting the comparison space to only $P-\dot{P}$ could play a significant role in the difference.

5.1.4 The power-law radio-emission model

We found the *power-law* exponents to be in range from 0.24 to 0.30 for the β and from -0.58 to -0.15 for the α . We see

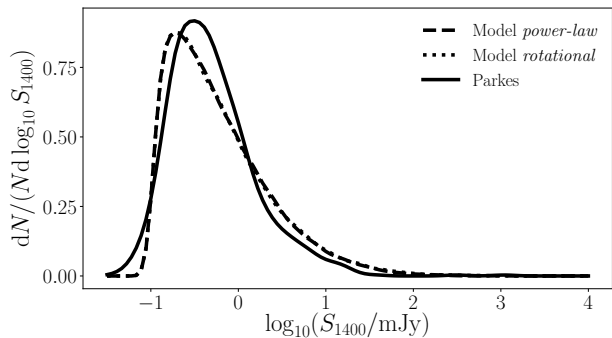


Figure 6. The comparison (upper plot) and difference (lower plot) of the distribution of the radio-flux of the observations, the *power-law* model, and the *rotational* model.

that our most probable values, $\alpha = -0.58$ and $\beta = 0.26$, are in $2\text{-}\sigma$ range of the results obtained by [Bates et al. \(2014\)](#): $\alpha = -1.12$ and $\beta = 0.28$. In comparison with ([Faucher-Giguère & Kaspi 2006](#)): $\alpha = -1.5$, $\beta = 0.5$, we differ more than 3 standard deviations. The difference can be explained by the inclusion of the magnetic field decay which does exhibit a strong correlation with other parameters describing the luminosity model (see Table 3 for α , β , γ , and Δ parameters), and an improved sampling of the parameter space.

5.1.5 The fit of radio luminosity laws

Although the fit in the 2D marginal distributions of the comparison space (second and third column of the Figure 5) seems to be in general agreement with the observations, the comparison of the radio-flux distribution (see Figure 6) shows some discrepancies. Our models underestimate the lower radio-fluxes, and overestimate the brightest objects. Both models behave in the same way pointing to a possible systematic error in the method, or model description. The coupling of the $P\text{-}\dot{P}\text{-}S$ in both the optimisation (comparison space), period evolution and radio-luminosity law, may have degenerated the problem – leading to too few observational constraints with regard to the number of free parameters. We also note that the introduction a phenomenological *death area* (see eq. 14) might have altered the distribution of pulsars in the $P\text{-}\dot{P}$ plane (see Figure 5). We excluded the parameter Ψ from our current analysis due to the complexity reduction of the computations. We plan to include the analysis of the death area in our future work.

5.1.6 The kicks distribution

We are aware that [Hobbs et al. \(2005\)](#) may be an imperfect distribution of the SN kicks, as stated in [Faucher-Giguère & Kaspi \(2006\)](#) or more recently in [Verbunt et al. \(2017\)](#). However, the spatial distribution (see section 2.4.2) is beyond the scope of this work. Moreover, by employing the Parkes Multibeam Survey, we focus only on the Galactic disk towards the centre of the Galaxy (see Table 4), thus limiting our study to a younger subset of the whole Galactic pop-

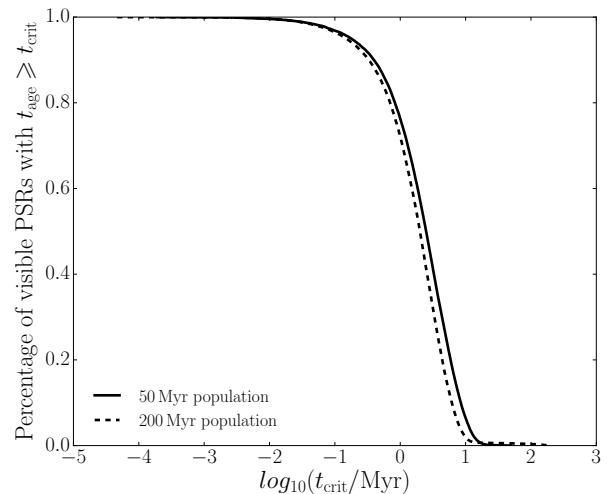


Figure 7. The cumulative distribution of the pulsars ages in the observed population. Lines – simulation limited to maximum age $t_{\text{age}} = 50$ Myr, Dots – simulation limited to maximum age $t_{\text{age}} = 200$ Myr

ulation. Any possible discrepancies in the kicks model are neglected by this choice.

5.1.7 Pulsar ages

We found that, within our model, a fraction of less than 1% of pulsars is older than 50 Myr (see Figure 7). Because those pulsars do not contribute in any significant way to the likelihood and as a result to MCMC and parameter estimation (a smaller 200-chains test yielded similar results to presented therein), we neglected this part of population. We limited the maximum age of pulsars to be $t_{\text{age}} \leq 50$ Myr. We do not contradict the observed kinematic ages distribution ([Noutsos et al. 2013](#)). Our study is focused on the Galactic disk population (see Table 4) and we are unable to effectively compare with older kinematic-population. Moreover, by the inclusion of the magnetic field decay, we greatly speed up the pulsars evolution track on the $P\text{-}\dot{P}$ plane. This may lead to incorrect comparison between the evolution (simulation) age and the characteristic age distribution. By computing the characteristic age

$$\tau = \frac{P}{2\dot{P}}, \quad (30)$$

we show in Figure 8 that the distribution of models resemble the observed sample and that it is possible to produce pulsars with $\tau \geq 50$ Myr.

5.1.8 Estimated SN rate

To derive the supernova rate from our models, we assume that the modelled and real populations have similar age ($t_{\text{max}} = 50$ Myr), and that the ratio of the number of visible

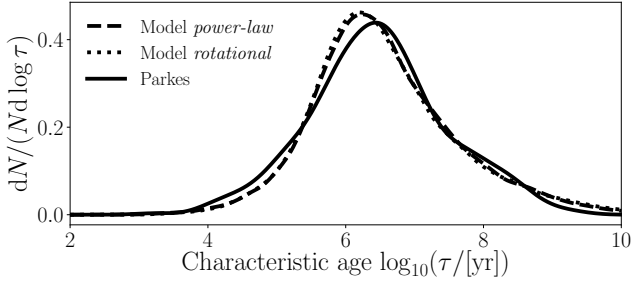


Figure 8. The probability density function of the characteristic age $\tau = P/(2\dot{P})$ in the reference *ATNF* subset for the Parkes Multibeam Survey and models.

| Parameter | Symbol | Value | Unit |
|-----------------------------|----------------------|-----------------------------------|--------------------|
| Receiver temperature | T_{rec} | 24 | K |
| Bandwidth | Δf | 288 | MHz |
| Number of polarizations | n_p | 2 | 1 |
| Frequency | f | 1400 | MHz |
| Sampling time | τ_{samp} | 0.00025 | s |
| Gain | G | 0.65 | K/Jy |
| Integration time | t_i | 2100 | s |
| Diagonal dispersion measure | DDM | 27.61 | pc/cm ³ |
| System loss | ι | 1. | 1 |
| Min. signal to noise ratio | $(S/N)_{\text{min}}$ | 10. | 1 |
| The sky coverage | | | |
| Galactic longitude range | | $-100^\circ \leq l \leq 50^\circ$ | |
| Galactic latitude range | | $-5^\circ \leq b \leq 5^\circ$ | |

Table 4. Parkes Multibeam Survey parameters.

pulsars N_{vis} to the total number of pulsars N_{tot} is constant:

$$\frac{N_{\text{vis}}^{\text{real}}}{N_{\text{tot}}^{\text{real}}} = \frac{N_{\text{vis}}^{\text{model}}}{N_{\text{tot}}^{\text{model}}}, \quad (31)$$

where $N_{\text{vis}}^{\text{model}}$ is the number of visible pulsars in a given model equal to 60012 and 58880 for the *power-law* and *rotational* models respectively, the $N_{\text{tot}}^{\text{model}}$ is the total number of simulated pulsars equal to $5.e6$, the $N_{\text{vis}}^{\text{real}}$ is the observed sample of pulsars equal to 969 pulsars, and the $N_{\text{tot}}^{\text{real}}$ is the total number of real pulsar and can be written as:

$$N_{\text{tot}}^{\text{real}} = t_{\text{max}} r_{\text{SN}}. \quad (32)$$

Where the r_{SN} is the supernova rate per century. Thus, we obtain our estimate:

$$r_{\text{SN}} = \frac{N_{\text{vis}}^{\text{real}} N_{\text{tot}}^{\text{model}}}{N_{\text{vis}}^{\text{model}} t_{\text{max}}}, \quad (33)$$

which yields:

$$r_{\text{SN}} = \begin{cases} 0.1615/100 \text{ yr} & \text{power-law model} \\ 0.1646/100 \text{ yr} & \text{rotational model} \end{cases} \quad (34)$$

Our estimate do not exceed the predicted rate of core-collapse supernova rate 0.5–1.1 per century (van den Bergh & Tammann 1991) as well the recent estimate based on INTEGRAL data for the combined type I b/c and type II supernova rate equal to 1.9 ± 1.1 per century (Diehl et al. 2006).

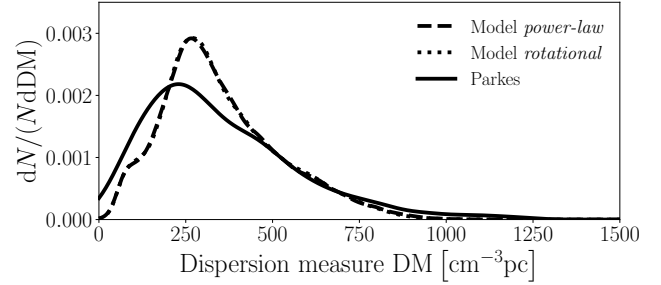


Figure 9. The probability density function of the dispersion measure in the reference *ATNF* subset for the Parkes Multibeam Survey and models.

5.1.9 The DM distribution

We limited our comparison space to three dimensions only – the period P and its derivative \dot{P} and the radio flux S_{1400} . Due to restriction on the computational time of the free electron distribution model of Yao et al. (2017) we excluded the geometrical part (galactic coordinates and dispersion measure) from our comparison space. Therefore we do not draw any conclusion about the pulsars spatial distribution in the Milky Way and their initial kicks, but the distances (in our case the dispersion measure) can have implication for the radio luminosity model. We present the model distribution of the dispersion measure and the one of the Parkes Multibeam Survey in Figure 9. The model distribution and the observed one are close even though they were not fitted.

5.2 Pulsar population with *Square Kilometre Array*

A very interesting consequence of the modelling presented here is the possibility to extend the results to the population of pulsars observable by the *Square Kilometre Array* (SKA). The SKA telescope is described in Carilli & Rawlings (2004), Staff & Array (2015), Kramer & Stappers (2015), and Grainge et al. (2017). We present the extrapolation of the observable pulsar population using the two models of pulsar luminosity considered above (the *power-law* model and *rotational* one) with their parameters set to the *most probable values* (see Table 2). We list two sets of probable parameters that describe the SKA for a mid-frequency survey in Table 5. The first one SKA-1-Mid represents our estimate of the initially planned SKA operation and the SKA-1-Mid-B a more pragmatic view of the parameters. To perform the extrapolation we compute a pulsar population of a given size (10^7) for the best set of parameters for both models. We infer what part of this population is seen in each survey (Parkes Multibeam, SKA-1-Mid, and SKA-1-Mid-B). We then compare the ratio of modelled pulsars seen in the Parkes Multibeam Survey to the cardinality of used subsection of the *ATNF* catalogue. This ratio is considered the normalisation constant W . In order to scale the artificial SKA observation we restrict the SKA-1-Mid and SKA-1-Mid-B surveys to the same part of the sky as the Parkes Multibeam Survey. Upon scaling the SKA surveys with the normalisation constant W we reach the estimated number of detectable single pulsars. We present the distribution of the detectable pulsars in the

| Parameter | Symbol | Value | Unit |
|-----------------------------|--------------------------|----------|--------------------|
| Receiver temperature | T_{rec} | 30 | K |
| Bandwidth | Δf | 300 | MHz |
| Number of polarizations | n_p | 2 | 1 |
| Frequency | f | 1400 | MHz |
| Sampling time | τ_{sampling} | 0.000064 | s |
| Gain | G | 15 (2) | K/Jy |
| Integration time | t_i | 2100 | s |
| Diagonal dispersion measure | DDM | 289.49 | pc/cm ³ |
| System loss | β | 1. | 1 |
| Min. signal to noise ratio | $(S/N)_{\text{min}}$ | 10. | 1 |

Table 5. SKA-1-Mid and SKA-1-Mid-B (in brackets) survey parameters.

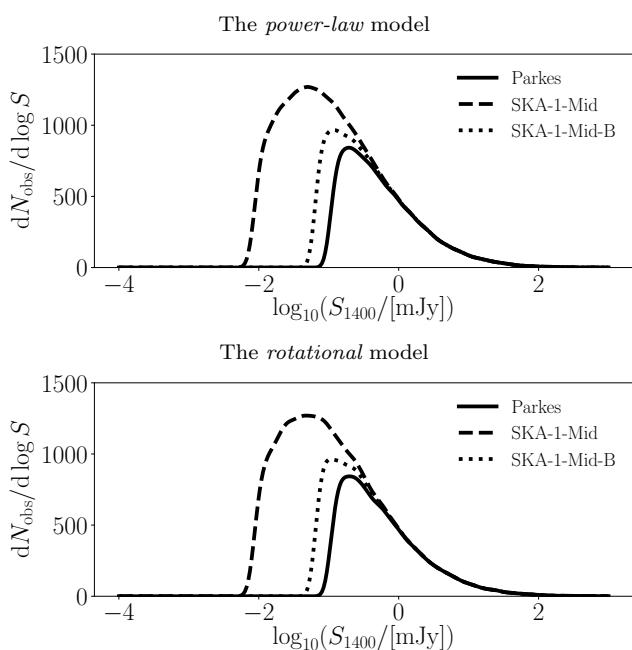


Figure 10. The distribution of pulsars radio-fluxes in the Parkes Multibeam Survey and the prediction for the SKA-1-Mid and SKA-1-Mid-B surveys. The total number of pulsars in N_{obs} is equal to 969 for Parkes with our selection cuts. In case of the SKA surveys the number of pulsars is 2364 and 2285 for the *power-law* and *rotational* model, respectively. For the *low-cost SKA* survey the number of pulsars is almost the same 1241 and 1229 for the *power-law* and *rotational* model, respectively.

function of the radio-flux at Figure 10. By our estimate, should the SKA observatory perform a survey of the same part of sky as the Parkes Multibeam Survey, we would reach an increase in detected radio pulsars by 23% or 137% for the SKA-1-Mid-B and SKA-1-Mid survey, respectively.

6 CONCLUSIONS

We presented a radio pulsar population synthesis model based on the one described by Faucher-Giguère & Kaspi (2006). We compared it with observations using the likelihood statistic and we used the Markov Chain Monte Carlo method to explore the parameter space. We used the recent model for the computation of the interstellar medium by Yao

et al. (2017). We compared the model with observations in the space spanned by period, period derivative, and radio flux. The pulsar initial parameters and their evolution are described by five parameters. We have explored two models with two different parametrizations of the pulsar luminosity: the *power-law* model described by three additional parameters and the *rotational* model described by two parameters. This allowed us to the estimation of the parameters and their confidence level. We found that the magnetic field decay is scale quite short and is approximately $3.63^{+0.94}_{-0.47}$ Myr in the *power-law* or $4.27^{+0.4}_{-0.38}$ Myr in the *rotational* model. The initial period distributions are centred around $\hat{P}_{\text{init}} \approx 30$ ms and 50 ms with widths of $\sigma_{P_{\text{init}}} \approx 40$ ms and 70 for the *power-law* and *rotational* model, respectively. The initial distribution of logarithm of magnetic field is almost identical in both models with the average $\log B_{\text{init}} \approx 12.66$ and $\log \sigma_{B_{\text{init}}} \approx 0.35$. We found that the preferred values of the exponents for the *power-law* radio-luminosity model are $\alpha = -0.37^{+0.22}_{-0.21}$ and $\beta = 0.26^{+0.04}_{-0.02}$, and for the model proportional to the rotational energy loss is $\kappa = 0.71^{+0.03}_{-0.04}$. Proposed parameters values differ from the works of Faucher-Giguère & Kaspi (2006), Popov et al. (2010), Gullón et al. (2014), and Bates et al. (2014). We contribute the difference to the inclusion of the radio-flux in the space that the main statistic (used to optimize the model) used as well as significantly large scope of the simulations (due to the increase of the available computational power).

In the view of the significant linear correlation between parameters exhibited by the *power-law* model, and the fact that two models lead to an almost identical population of observed pulsars, we believe that the *rotational* model should be preferred. We note, that even the *rotational* model has some non-negligible correlation between magnetic field decay time-scale and parameters describing the initial distribution of magnetic field. To shed some light on the possible cause of the parameters correlation, additional constraints from the observation should be provided, and more sophisticated description of the radio luminosity implemented.

We estimated the number of new observable pulsars, should the SKA survey cover the same area, as the Parkes Multibeam Survey to be increased by 23–137% depending on the final parameters of the SKA survey. We release the *Indri* code⁶ used in this research in hopes of contributing to the advancement of *dynamical* models in the pulsar population synthesis research field.

ACKNOWLEDGEMENTS

Marek Cieřlar and Tomasz Bulik were supported by the NCN Grant No. UMO-2014/14/M/ST9/00707. Marek Cieřlar acknowledges support from Polish Science Foundation *Master2013* Subsidy as well as from the NCN Grant No. 2016/22/E/ST9/00037. Tomasz Bulik is grateful for support from TEAM/2016-3/19 from the FNP. Stefan Osłowski acknowledges support from the Alexander von Humboldt Foundation and ARC grant Laureate Fellowship FL150100148.

⁶ <http://github.com/cieslar/Indri>

In our work we used the Mersenne Twister pseudo random number generator by [Matsumoto & Nishimura \(1998\)](#). We thank Michał Bejger and Paweł Cieciełag from Nicolaus Copernicus Astronomical Center (Polish Academy of Sciences, Warsaw) for housing part of our simulations on the *bigdog* cluster located at the Institute of Mathematics (Polish Academy of Sciences, Warsaw). The majority of the computations were performed on the OzSTAR national facility at Swinburne University of Technology. OzSTAR is funded by Swinburne University of Technology and the National Collaborative Research Infrastructure Strategy (NCRIS).

REFERENCES

- Arzoumanian Z., Chernoff D. F., Cordes J. M., 2002, *ApJ*, 568, 289
- Bates S. D., Lorimer D. R., Rane A., Swiggum J., 2014, *MNRAS*, 439, 2893
- Belczynski K., Benacquista M., Bulik T., 2010, *ApJ*, 725, 816
- Beskin V. S., Chernov S. V., Gwinn C. R., Tchekhovskoy A. A., 2015, *Space Sci. Rev.*, 191, 207
- Bhat N. D. R., Cordes J. M., Camilo F., Nice D. J., Lorimer D. R., 2004, *ApJ*, 605, 759
- Blondin J. M., Mezzacappa A., 2007, *Nature*, 445, 58
- Carilli C. L., Rawlings S., 2004, *New Astron. Rev.*, 48, 979
- Cordes J. M., Lazio T. J. W., 2002, ArXiv Astrophysics e-prints
- Cordes J. M., Lazio T. J. W., 2003, ArXiv Astrophysics e-prints
- Dewey R. J., Taylor J. H., Weisberg J. M., Stokes G. H., 1985, *ApJ*, 294, L25
- Diehl R., et al., 2006, *Nature*, 439, 45
- Faucher-Giguère C.-A., Kaspi V. M., 2006, *ApJ*, 643, 332
- Foreman-Mackey D., Hogg D. W., Lang D., Goodman J., 2013, *PASP*, 125, 306
- Gilks W. R., Best N., Tan K., 1995, *Applied Statistics*, pp 455–472
- Gold T., 1968, *Nature*, 218, 731
- Gonthier P. L., Story S. A., Clow B. D., Harding A. K., 2007, *Ap&SS*, 309, 245
- Goodman J., Weare J., 2010, *Communications in Applied Mathematics and Computational Science*, Vol. 5, No. 1, p. 65-80, 2010, 5, 65
- Grainge K., et al., 2017, *Astronomy Reports*, 61, 288
- Gullón M., Miralles J. A., Viganò D., Pons J. A., 2014, *MNRAS*, 443, 1891
- Hastings W. K., 1970, *Biometrika*, 57, 97
- Hewish A., Bell S. J., Pilkington J. D. H., Scott P. F., Collins R. A., 1969, *Nature*, 224, 472
- Hobbs G., Lorimer D. R., Lyne A. G., Kramer M., 2005, *MNRAS*, 360, 974
- Igoshev A. P., Popov S. B., 2015, *Astronomische Nachrichten*, 336, 831
- Kiel P. D., Hurley J. R., 2009, *MNRAS*, 395, 2326
- Kiel P. D., Hurley J. R., Bailes M., Murray J. R., 2008, *MNRAS*, 388, 393
- Kramer M., Stappers B., 2015, *Advancing Astrophysics with the Square Kilometre Array (AASKA14)*, p. 36
- Levin L., et al., 2013, *MNRAS*, 434, 1387
- Lorimer D. R., 2011, in Torres D. F., Rea N., eds, *High-Energy Emission from Pulsars and their Systems*. p. 21 ([arXiv:1008.1928](#)), doi:10.1007/978-3-642-17251-9_2, <http://adsabs.harvard.edu/abs/2011heep.conf...21L>
- MacKay D., 2003, *Information Theory, Inference and Learning Algorithms*. Cambridge University Press
- Manchester R. N., et al., 2001, *MNRAS*, 328, 17
- Manchester R. N., Hobbs G. B., Teoh A., Hobbs M., 2005, *AJ*, 129, 1993
- Maron O., Kijak J., Kramer M., Wielebinski R., 2000, *A&AS*, 147, 195
- Marsaglia G., 1972, *Ann. Math. Statist.*, 43, 645
- Matsumoto M., Nishimura T., 1998, *ACM Trans. Model. Comput. Simul.*, 8, 3
- Miyamoto M., Nagai R., 1975, *PASJ*, 27, 533
- Mosegaard K., Tarantola A., 1995, *J. Geophys. Res.*, 100, 12
- Narayan R., Ostriker J. P., 1990, *ApJ*, 352, 222
- Noutsos A., Schnitzeler D. H. F. M., Keane E. F., Kramer M., Johnston S., 2013, *MNRAS*, 430, 2281
- Ořłowski S., Bulik T., Gonddek-Rosińska D., Belczyński K., 2011, *MNRAS*, 413, 461
- Ostriker J. P., Gunn J. E., 1969, *ApJ*, 157, 1395
- Pacini F., 1967, *Nature*, 216, 567
- Paczynski B., 1990, *ApJ*, 348, 485
- Popov S. B., Prokhorov M. E., 2007, *Physics Uspekhi*, 50, 1123
- Popov S. B., Pons J. A., Miralles J. A., Boldin P. A., Posselt B., 2010, *MNRAS*, 401, 2675
- Rantsiou E., Burrows A., Nordhaus J., Almgren A., 2011, *ApJ*, 732, 57
- Rudak B., Ritter H., 1994, *MNRAS*, 267, 513
- Scott D. W., 2015. John Wiley & Sons
- Shapiro S. L., Teukolsky S. A., 1986, *Black Holes, White Dwarfs and Neutron Stars: The Physics of Compact Objects*. <http://adsabs.harvard.edu/abs/1986bhwd.book.....S>
- Sharma S., 2017, *ARA&A*, 55, 213
- Staff S. O., Array S., 2015, *Advancing Astrophysics with the Square Kilometer Array*. Dolman Scott Limited
- Tarantola A., 2005, *Inverse Problem Theory and Methods for Model Parameter Estimation*. EngineeringPro collection, Society for Industrial and Applied Mathematics
- Tauris T. M., Manchester R. N., 1998, *MNRAS*, 298, 625
- Verbunt F., Igoshev A., Cator E., 2017, *A&A*, 608, A57
- Verlet L., 1967, *Physical Review*, 159, 98
- Wainscoat R. J., Cohen M., Volk K., Walker H. J., Schwartz D. E., 1992, *ApJS*, 83, 111
- Yao J. M., Manchester R. N., Wang N., 2017, *ApJ*, 835, 29
- Yusifov I., Küçük I., 2004, *A&A*, 422, 545
- Zhang C. M., Kojima Y., 2006, *MNRAS*, 366, 137
- van den Bergh S., Tammann G. A., 1991, *ARA&A*, 29, 363

APPENDIX A:

In this appendix, for the completion purpose, we present the parts of the model that are identical to the model developed by [Faucher-Giguère & Kaspi \(2006\)](#).

A1 The Milky Way

A1.1 The Galactic potential

We use the well-established three-component Galactic potential consisting of the disk, the bulge and the halo. The bulge Φ_{Bulge} and the disk Φ_{Disk} gravitational potentials are adopted after [Miyamoto & Nagai \(1975\)](#). The formula describing the bulge is:

$$\Phi_{\text{Bulge}} = -\frac{GM_b}{\sqrt{b_b^2 + r^2}} \quad (\text{A1})$$

where $M_b = 1.12 \times 10^{10} M_{\odot}$ and $b_b = 0.277 \text{ kpc}$, and $r = (x^2 + y^2 + z^2)^{1/2}$. We model the disk potential as:

$$\Phi_{\text{Disk}} = -\frac{GM_d}{\sqrt{(a_d + \sqrt{b_d^2 + z^2})^2 + \rho^2}} \quad (\text{A2})$$

| Arm | k rad | ρ_0 kpc | θ_0 rad |
|--------------------|---------|--------------|----------------|
| Norma | 4.25 | 3.48 | 1.57 |
| Carina-Sagittarius | 4.25 | 3.48 | 4.71 |
| Perseus | 4.89 | 4.90 | 4.05 |
| Crux-Scutum | 4.89 | 4.90 | 0.95 |

Table A1. Spiral arms parameters.

where $M_d = 8.78 \times 10^{10} M_\odot$, $a_d = 4.2$ kpc and $b_d = 0.198$ kpc, and $\rho = (x^2 + y^2)^{1/2}$. We use the halo potential Φ_{Halo} following the model of Paczynski (1990):

$$\Phi_{\text{Halo}} = -\frac{GM_h}{2r_c} \left(2\frac{r_c}{r} \arctan\left(\frac{r}{r_c}\right) + \log\left(\frac{r^2}{r_c^2} + 1\right) \right) \quad (\text{A3})$$

where $M_h = 5 \times 10^{10} M_\odot$, $r_c = 6$ kpc. As the associated density of the halo is diverging so we cut the halo potential at $r_{\text{cut}} = 100$ kpc, see e.g. Belczynski et al. (2010). We neglect the dependence of the galactic potential on the individual Galactic arms.

A1.2 The initial positions of pulsars

We adopt the initial position distribution after Faucher-Giguère & Kaspi (2006) with the assumption that pulsars are born inside the galactic spiral arms. Following them, we exclude the Local Arm as the origin of the pulsars. The centroids of each arm are described as logarithmic spirals (Wainscoat et al. 1992):

$$\theta(\rho) = k \log\left(\frac{\rho}{\rho_0}\right) + \theta_0 \quad (\text{A4})$$

with their parameters listed in the Table A1. With equal probability we chose the arm in which pulsar is born. The distance ρ_{raw} from the centre of the Galaxy is drawn using the stellar surface density distribution in the Galactic plane (Yusifov & Küçük 2004):

$$\xi(\rho_{\text{raw}}) \sim \left(\frac{\rho_{\text{raw}} + R_1}{R_\odot + R_1}\right)^a \exp\left(-b\left(\frac{\rho_{\text{raw}} - R_\odot}{R_\odot + R_1}\right)\right) \quad (\text{A5})$$

where $a = 1.64$, $b = 4.01$, $R_1 = 0.55$ kpc, and $R_\odot = 8.5$ kpc is the distance of the Sun from the Galactic centre. We insert the radial distance into equation A4 to obtain the position along the spiral arm's centroid $(\rho_{\text{raw}}, \theta_{\text{raw}})$. This position is then smeared by adding a correction to the angle θ_{raw} to avoid artificial structures in the Galactic centre:

$$\theta_{\text{wide}} = \theta_{\text{raw}} + \theta_{\text{corr}} \exp\left(\frac{-0.35\rho_{\text{raw}}}{\text{kpc}}\right) \quad (\text{A6})$$

where θ_{corr} is randomly chosen from the interval of $[0, 2\pi]$ radians. We introduce the internal structure of spiral arms by displacing the initial radial position of the pulsar in the galactic plane. We add a vector with random direction and a length drawn from a Gaussian distribution with $\sigma = 0.07\rho_{\text{raw}}$. The resulting initial position distribution in the Galactic plane is shown in the Figure A1. The vertical position of the pulsar is drawn from the exponential distribution with the mean $\langle z_0 \rangle = 0.05$ kpc. We populate the Galaxy with stars by rotating spiral arms and inserting pulsars uniformly in time from their maximal simulated age, $\max(t_{\text{age}}) = 50$ Myr ago, to a present day. We assume a simple, rigid Galactic rotation with the period of $P_{\text{rot}} = 250$ Myr:

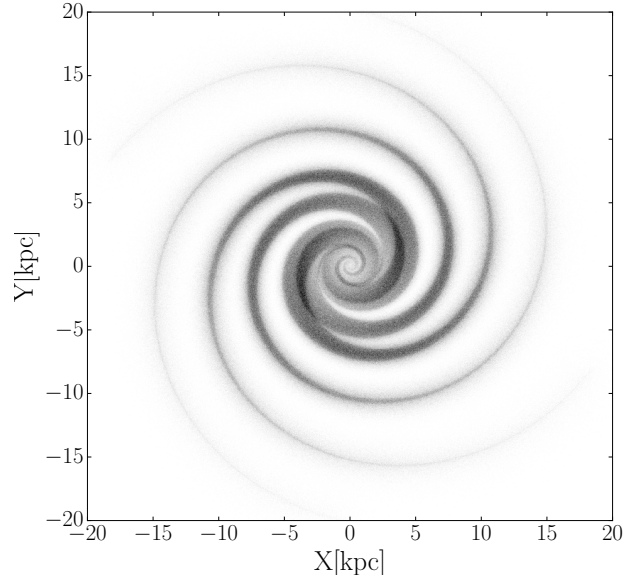


Figure A1. Spiral Arms – initial positions distribution in the Galactic plane of randomly drawn, 10^7 pulsars.

$$\theta = \theta_{\text{wide}} - 2\pi t_{\text{age}}/P_{\text{rot}} \quad (\text{A7})$$

We justify the rigid rotation assumption with the maximum possible age of a modelled pulsar $\max(t_{\text{age}}) = 50$ Myr being significantly lower than the rotation period of the Galaxy. For the discussion of this assumption see section 5.1.7.

A1.3 The initial velocity

At birth, each pulsar is subjugated to a kick due to the supernova explosion resulting in change in the initial velocity. We use the model of Hobbs et al. (2005) to draw the absolute value of the kicks velocity from a one-dimensional Maxwellian distribution with a mean $\langle v \rangle = 265$ km/s:

$$\mathcal{P}_{\text{kick}}(v) = \sqrt{\frac{2}{\pi}} \frac{v^2}{\langle v \rangle^3} \exp\left(\frac{-v^2}{2\langle v \rangle^2}\right) \quad (\text{A8})$$

and a random direction. For the uniform spherical distribution of points we employ the algorithm of Marsaglia (1972). The resulting kick vector is added to the Keplerian motion in the Galactic potential at the neutron stars birth position.

A2 The neutron star physics

A2.1 The rotation evolution

To describe the spin-down process we use the canonical lighthouse model (Ostriker & Gunn 1969). It approximates the pulsar with magnetic dipole rotating in a vacuum and assumes that the total loss of the rotation energy is emitted in the electromagnetic spectrum. This leads to the following relation between magnetic field induction, period and period derivative (for details refer to Shapiro & Teukolsky (1986)

chapter 10.5):

$$B = \left(\frac{3Ic^3 P \dot{P}}{8\pi^2 R_{\text{NS}}^6} \right)^{1/2} = \eta(P\dot{P})^{1/2} \quad (\text{A9})$$

for a perpendicular rotator, where $\eta \simeq 3.2 \times 10^{19} \text{ G s}^{-1/2}$.

A2.2 The initial parameters of pulsars

We adopted initial spin period distribution and magnetic field strength from the optimal model by [Faucher-Giguère & Kaspi \(2006\)](#). In case of the period it is a positive normal distribution (we redraw negative values) centred at $\widehat{P}_{\text{init}}$ and with standard deviation $\sigma_{P_{\text{init}}}$. We initialise the magnetic field strength with values drawn from log-normal distribution centred at a value of $\log(\widehat{B}_{\text{init}})$ and with standard deviation $\log(\sigma_{B_{\text{init}}})$. All four variables presented above are used to parametrize the evolution model. We list their limits in the Table 1.

A3 Radio Properties

A3.1 The minimal detectable flux

We follow identical prescription as [Osłowski et al. \(2011\)](#) to model radio selection effects. The minimal detectable flux of a pulsar is described by the radiometer equation ([Dewey et al. 1985](#)) adjusted for pulsating sources:

$$S_{\text{min}} = \frac{\iota (S/N)_{\text{min}} T_{\text{sys}}}{G \sqrt{n_p t_i \Delta f}} \sqrt{\frac{W_e}{P - W_e}} \quad (\text{A10})$$

where the ι is a value describing *system loss*, T_{sys} is the system temperature, G is the gain, n_p represents the number of polarizations, Δf is the bandwidth, t_i is the integration time, $(S/N)_{\text{min}}$ represents the minimal signal to noise ratio, W_e is the effective width of the pulse and P is the pulsar spin period. We supply the formula with values appropriate to the Parkes Multibeam Survey (see Table 4). For the system temperature T_{sys} we consider only the sky temperature T_{sky} in the direction of the measurement and the receiver noise temperatures T_{rec} :

$$T_{\text{sys}} = T_{\text{rec}} + T_{\text{sky}} \quad (\text{A11})$$

The effective width of the pulse W_e is a function of the intrinsic width W_i , the sampling time τ_{samp} , the pulsar dispersion measure DM, the diagonal dispersion measure DDM (characteristic to the survey) and the interstellar scattering time τ_{scatt} describing the pulse widening due to the multipath propagation (dissipation of the signal by the free electron clouds in the Galaxy). The effective width W_e formula takes form of:

$$W_e^2 = W_i^2 + \tau_{\text{samp}}^2 + \left(\tau_{\text{samp}} \frac{\text{DM}}{\text{DDM}} \right)^2 + \tau_{\text{scatt}}^2 \quad (\text{A12})$$

We obtained the interstellar scattering time τ_{scatt} using the model developed by [Bhat et al. \(2004\)](#) in which τ_{scatt} is a function of the dispersion measure DM. The minimal flux S_{min} , the effective width W_e , the system temperature T_{sys} and $\tau_{\text{scattering}}$ were calculated using the functions from the

PSREVOLVE⁷ code developed at the Centre for Astrophysics and Supercomputing, Swinburne University of Technology.

This paper has been typeset from a $\text{T}_{\text{E}}\text{X}/\text{L}^{\text{A}}\text{T}_{\text{E}}\text{X}$ file prepared by the author.

⁷ <http://astronomy.swin.edu.au/~fdonea/psrevolve.html>